

Magnetic Transitions in Exotic Perovskites

Stabilized by Chemical and Physical Pressure

*Yalin Ma,¹ Maxim S. Molokeev,^{2,3,4} Chuanhui Zhu,¹ Shuang Zhao,¹ Yifeng Han,¹ Meixia Wu,¹
Mark Croft,⁵ Man-Rong Li^{*,1}*

¹ Key Laboratory of Bioinorganic and Synthetic Chemistry of Ministry of Education, School of Chemistry, Sun Yat-Sen University, Guangzhou 510275, China

² Laboratory of Crystal Physics, Kirensky Institute of Physics, Federal Research Center KSC SB RAS, Krasnoyarsk 660036, Russia

³ Siberian Federal University, Krasnoyarsk 660041, Russia

⁴ Department of Physics, Far Eastern State Transport University, Khabarovsk 680021, Russia

⁵ Department of Physics & Astronomy, Rutgers, The State University of New Jersey, 136 Frelinghuysen Road, Piscataway, New Jersey 08854, United States

ABSTRACT

Exotic Perovskites significantly enrich materials in multiferroic and magnetoelectric applications. However, their design and synthesis are the challenge due to the mostly required extreme conditions at high pressure. Herein, we have presented the $\text{Ca}_{2-x}\text{Mn}_x\text{MnTaO}_6$ ($0 \leq x \leq 1.0$) solid solutions stabilized by chemical pressure assisted with intermediate physical pressure up to 7 GPa. The incorporation of Mn^{2+} into the *A*-site neither drives any cationic ordering nor modifies the orthorhombic *Pbnm* structure, namely written as $(\text{Ca}_{1-x/2}\text{Mn}_{x/2})(\text{Mn}_{1/2}\text{Ta}_{1/2})\text{O}_3$ with disordered *A* and *B* site cationic arrangements. The increment of x is accompanied by a ferromagnetic to antiferromagnetic transition around $x = 0.2$, which is rooted in the super-exchange interactions between *A*-site Mn^{2+} and *B*-site Mn^{3+} . Partial charge disproportionation of the *B*-site Mn^{3+} into Mn^{2+} and Mn^{4+} occurs for x above 0.8 samples as manifested by X-ray spectrum and magnetic behaviors. The coexistence of *B*-site Mn^{3+} (Jahn-Teller distortion ion) and *B'*-site Ta^{5+} (second-order Jahn-Teller distortion ion) could be energetically responsible for the absence of *A*-site columnar ordering as observed in other quadruple perovskites with half of the *A*-sites occupied by small transition-metal cations. These exceptional findings indicate that exotic perovskites can be successfully stabilized chemical and intermediate physical pressure, and the presence of John-teller distortion cations at the same lattice should be avoid to enable cationic ordering.

INTRODUCTION

Perovskite oxides have attracted great interest because of their enriched structural, magnetic and electronic properties.¹⁻⁴ The stability and crystal system of ABO_3 perovskites can be depicted by the octahedral factor $\mu = r_B/r_O$ and tolerance factor $t = (r_A + r_O)/\sqrt{2}(r_B + r_O)$ proposed by Goldschmidt (r_i stands for the ionic radius of ion i).^{5,6} The radii of ions and tilting of octahedron have a significant impact on stabilizing perovskite structure in light of their chemical, octahedral, stretch, and tilt limits.⁷⁻¹² In contrast to conventional perovskite with large A -site cations, the exotic perovskite can adaptively incorporate small cations (especially transition-metal ions) into the A -site.¹³⁻¹⁶ A -site columnar-ordered quadruple perovskites $A_2A'A''B_4O_{12}$ with 50% of the small A -sites (denoted as square-planar coordinated A' and tetrahedrally coordinated A'' , respectively) was firstly discovered in $Ca_2Fe'Fe''Ti_4O_{12}$ (also known as $CaFeTi_2O_6$ with $A' = A'' = Fe$)¹⁷ and then $Ca_2Mn'Mn''Ti_4O_{12}$ (known as $CaMnTi_2O_6$ with $A' = A'' = Mn$).¹⁸ $Ca_2Fe'Fe''Ti_4O_{12}$ crystallizes in centrosymmetric $P4_2/nmc$ (No. 137), while $Ca_2Mn'Mn''Ti_4O_{12}$ adopts a polar $P4_2mc$ (No. 105) structure in that Mn' displaces off from the $Mn'O_4$ square-plane (**Figure 1a**) other than exactly stays in the oxygen plane as observed for Fe' in $Fe'O_4$ in $Ca_2Fe'Fe''Ti_4O_{12}$.¹⁹ Rock-salt B -sites ordering in $A_2A'A''B_2B'_2O_{12}$ (**Figure 1b**) provides higher compositional freedom as reported in the $P4_2/n$ (No. 86) type $Ca_2Mn'Mn''B_2Re_2O_{12}$ ($B = Mn$,²⁰ Fe ,²⁰ Co ,²¹ Ni), $Ca_2Mn^{A'}Cu^{A''}(Fe_2)^B(Re_2)^{B'}O_{12}$,²⁰ and $R_2Mn'Mn''Mn_2Sb_2O_{12}$ ($R = La, Pr, Nd, Sm$).²² The $A'O_4$ (square-planar), $A''O_4$ (tetrahedral), BO_6 (octahedral), and $B'O_6$ (octahedral) sites in $A_2A'A''B_2B'_2O_{12}$ are highly adaptable,²³ and can be occupied by the same element as recently observed in RMn_3O_6 ($R = Y, Gd, Dy, Ho, Er, Tm$; $A' = A'' = B = B' = Mn$),²⁴⁻²⁶ which crystallize in $Pm\bar{m}n$ (No. 59, **Figure 1c**) and can be structurally written as $R^{3+}_2(Mn^{2+})^{A'}(Mn^{3+})^{A''}(Mn^{3+})_2^B(Mn^{3.5+})_2^{B'}O_{12}$ with layered charge ordering over the B -sites. When

75% of the *A*-sites are occupied by small cations, $AA'_3B_4O_{12}$ -type quadruple perovskites can be formed with square-planar coordinated *A'*-site, such as $A' = Mn^{3+}, Co^{2+}, Cu^{2+}, Pd^{2+}$ in $LaMn_3V_4O_{12}$,²⁷ $LaCu_3Fe_4O_{12}$,²⁸ $CaCo_3V_4O_{12}$,^{29, 30} $CaPd_3Ti_4O_{12}$,^{31, 32} respectively. Most known $AA'_3B_4O_{12}$ quadruple perovskites are in cubic *Im*-3 (No. 204) symmetry (**Figure 1d**) unless the *B*-site charge-ordering induced distortion occurs as in rhombohedral manganites $A^{2+}Mn_3Mn_4O_{12}$ (*R*-3, No. 148, $A = Ca, Cd, Pb, Pr, Sr$, **Figure 1e**).³³⁻³⁵ 1322-type *B*-site ordering of quadruple perovskites $AA'_3B_2B'_2O_{12}$ leads to a symmetry evolution from *Im*-3 to *Pn*-3 (No. 201, **Figure 1f**) such as reported in $CaCu_3Fe_2Re_2O_{12}$,³⁶ $CaCu_3Fe_2Nb_2O_{12}$,³⁷ and $NaCu_3Fe_2Os_2O_{12}$.³⁸ In $A^{3+}Mn_7O_{12}$ ($A = La, Pr, Nd$) series the trivalent *A*-site ion drives more Jahn-Teller distorted Mn^{3+} component on the *B*-site, which, together with charge ordering, results in monoclinic *I2/m* (No. 12) structure (**Figure 1g**) as in $Pr^{3+}Mn^{3+}_3(Mn^{2.99+})_2(Mn^{3.01+})_2O_{12}$.^{39, 40} The spatial effect of $6s^2$ -lone pair electrons of Bi^{3+} in $BiMn_7O_{12}$ further leads to complex temperature-dependent symmetry evolution of *Im*-3 (above 608 K) - *I2/m* (460-608 K) - *Im* (290-460 K) - *P1* (below 290 K) upon cooling.⁴¹ Full occupation of the *A*-site with small cations usually draws pressure-dependent polymorph competition, and mostly the perovskite phases need to be stabilized from higher pressure synthesis.^{16, 42-44} $GdFeO_3$ -based *Pnma* (No. 62, **Figure 1h**) and *P2₁/n* (No. 14) structures (**Figure 1i**) have been successively discovered in ABO_3 -type (such as $MnVO_3$ and $ScCrO_3$)⁴⁵⁻⁴⁷ and $A_2BB'O_6$ -type (such as Mn_2BSbO_6 ($B = Fe$,⁴³ Sc ,⁴⁸ V ⁴⁹), Mn_2BReO_6 ($B = Mn$,^{14, 50} Fe ,^{15, 51} Co ⁵²), and $Mn_2(Fe_{0.8}Mo_{0.2})MoO_6$)¹³) perovskites, respectively. $AA'_3B_4O_{12}$ -type quadruple perovskites can also be prepared in this catalog if the pressure is high enough, such as $ACu_3V_4O_{12}$ (*Im*-3, $A = Cu, Mn$), and ζ - Mn_2O_3 (structurally written as $Mn^{2+}(Mn^{3+})_3(Mn^{3.25+})_4O_{12}$, **Figure 1j**, *P*-1 (No. 2)).⁵³⁻⁵⁵ Post-perovskite structural compounds (**Figure 1k**, *Cmcm*, No. 63) such as δ - Mn_2O_3 and $MgSiO_3$ can exist at extremely high pressure but unquenchable to ambient

conditions.^{56, 57}

Partial or full occupation of small cations on the A-site in exotic perovskite not only depicts an enriched image of structural chemistry, but also provides a continuous impetus to search for emergent physical properties, in that the small A-site cations, especially transition-metal ions, enhance the quantum degree of freedom such as lattice, spin, charge, and orbital. The reduced t can cause structural distortion and thus large spontaneous electrical polarization (P_S) in noncentrosymmetric materials,^{58, 59} while the transition-metal-rich lattices lead to robust magnetic interplays and thus magnetoelectric effect.^{15, 28, 51} For examples, $\text{CaMnTi}_2\text{O}_6$ is the only lone-pair-electron free switchable ferroelectric double perovskite ($P_S \sim 24 \mu\text{C}/\text{cm}^2$),¹⁸ demonstrating potential piezoelectric and ferroelectric-photovoltaic applications; $\text{Ca}_2\text{Mn}^{A'}\text{Cu}^{A''}(\text{Fe}_2)^B(\text{Re}_2)^{B'}\text{O}_{12}$ is an above room-temperature ferromagnet (Curie temperature T_C of 560 K) with large room-temperature magnetizations and low-temperature switchable magnetoresistance;²⁰ $\text{LaCu}_3\text{Fe}_4\text{O}_{12}$ undergoes a temperature-dependent charge transfer around 400 K, accompanied by a metal-insulator transition behavior;²⁸ $\text{CaCu}_3\text{Fe}_2\text{Re}_2\text{O}_{12}$ is a ferrimagnetic ($T_C \sim 560$ K) half metal with large saturated magnetization of $8.7 \mu_B$;³⁶ $\text{Mn}_2\text{FeReO}_6$ displays giant positive magnetoresistance up to 220%;^{15, 51} $\zeta\text{-Mn}_2\text{O}_3$ is the hardest direct narrow bandgap semiconductor, showing switchable p - n electronical conduction and spin-induced multiferroicity.⁵³⁻⁵⁵ This list can be even longer. However, these exotic perovskites are thermodynamically metastable and need to be prepared at high-pressure (usually above 6 GPa) and temperature (HPT). This costly procedure and small-scale sample amount (usually milligram level) significantly limit the applications of these materials. Therefore, synthesis at ambient or much lower pressure, which remains a challenge, is highly desired.

Recently, Zhou *et al.* successfully stabilized gram-level high-pressure $\text{Ca}_{2-x}\text{Mn}_x\text{Ti}_2\text{O}_6$ ($x \leq 0.6$) phase under a very modest pressure (below 0.1 GPa).¹⁹ $\text{Ca}_{1.4}\text{Mn}_{0.6}\text{Ti}_2\text{O}_6$ is isostructural with $\text{CaMnTi}_2\text{O}_6$ ($P4_2mc$) and shows similarly high ferroelectric transition temperature. These findings suggest that it is possible to achieve large-scale high-pressure product driven by chemical potential (pressure)⁶⁰ and very modest physical pressure. Understandably, Ca^{2+} and Mn^{2+} have the same charge and comparable ionic radii (at eight coordination, $^{\text{VIII}}r(\text{Ca}^{2+}) = 1.12$ Å, $^{\text{VIII}}r(\text{Mn}^{2+}) = 0.96$ Å),⁶¹ so that the chemical pressure and geometric homogeneity can assist to underpin Mn^{2+} in the Ca^{2+} matrix. In this work we reported the perovskite solid solutions of $\text{Ca}_{2-x}\text{Mn}_x\text{MnTaO}_6$ ($0 \leq x \leq 1.0$) stabilized by the combination of chemical and physical pressure, and intensively studied the composition-dependent evolution of the crystal structure, formal oxidation states of cations, and magnetic properties.

EXPERIMENTAL SECTION

Synthesis. The $\text{Ca}_2\text{MnTaO}_6$ (CMTO) precursor was prepared by solid-state reactions with appropriate stoichiometric amount of CaCO_3 (MACKLIN, 99.99%), Mn_2O_3 (Sigma-Aldrich, 99.99%), and Ta_2O_5 (Alfa Aesar, 99.993%). The mixture was ground and pressed into pellets, calcined at 1275 K for 8 h to decompose the carbonate. Then, the product was reground and pressed into pellets, sintered in air for two periods of 48 h at 1653 K with intermediate grinding and pelletizing. $\text{Ca}_{2-x}\text{Mn}_x\text{MnTaO}_6$ samples with $x = 0.2, 0.4, 0.6, 0.8, 1.0, 1.5, 1.6$ and 2.0 were synthesized from the stoichiometric mixtures of the as-prepared CMTO, MnO (Alfa Aesar, 99.99%), Mn_2O_3 , and Ta_2O_5 . Samples with $x = 0.2$ were heated at 1625 K for 24 h under ambient pressure (AP), whereas $x = 0.4 - 2.0$ were prepared in a Walker-type multi-anvil apparatus at

1523-1625 K under 5-8 GPa for 30 min in Pt capsules and then quenched to room temperature, followed by a gradual release of the pressure.

X-ray Powder Diffraction and Energy Dispersive X-ray Spectroscopy. X-ray powder diffraction (XRD) data were collected at room temperature on a RIGAKU RINT-2000 diffractometer by using Cu-K α radiation ($\lambda = 1.5418 \text{ \AA}$). Here the 2θ range between 10° and 120° with a step size of 0.02° was measured, using a counting time of 0.24 s per step at 40 kV and 26 mA. The TOPAS 4.2 software package⁶² was applied to perform diffraction data analysis and Rietveld refinement. Cross sectional scanning electron microscopy (SEM) with energy-dispersive X-ray spectroscopy (EDS) images were recorded using a FEI Quanta 400F with an Oxford-instruments INCA 400 EDS detector operating at an accelerating voltage of 20 kV. EDS elemental composition could be expressed quantitatively as weight percentage or atomic percentage.

X-ray Absorption Near Edge and Photoelectron Spectroscopy. Mn-K and Ta-L_{2,3} X-ray absorption near edge spectroscopy (XANES) data were collected in both the fluorescence and the transmission modes with simultaneous standards. All of the spectra were fit to linear pre- and post-edge backgrounds and normalized to the unity absorption step across the edge.^{13, 63, 64} The Ca_{1.8}Mn_{0.2}MnTaO₆ XANES measurements was performed on at the Brookhaven NSLS-II on the QAS 7-BM beamline using a Si-111 channel cut monochromator. Most of the standard spectra were performed at X-19A at NSLS-I with a Si-111 double crystal monochromator. X-ray photoelectron spectroscopy (XPS) was performed on a Nexsa XPS system equipped with a monochromatic Al K α X-ray source ($h\nu = 1486.6 \text{ eV}$) operated at 720 W, and background

pressure was kept about 2×10^{-9} mbar. All binding energies were calibrated using surface contaminant carbon ($C 1s = 284.8$ eV) as a standard to scale.

Magnetic Measurements. Magnetic measurements were implemented with a Physical Properties Measurement System (PPMS, Quantum Design). The temperature-dependent magnetization was measured in zero field cooled (ZFC) and field cooled (FC) modes in a temperature scope of 5-400 K under 0.1 T magnetic field (H). Field dependence of isothermal magnetization was measured under an applied magnetic field varying from -5 to 5 T between 5 and 300 K.

RESULTS AND DISCUSSION

Synthesis and Structural Characterization.

The degree of cationic ordering and octahedral tilting in double perovskite oxides kinetically depends on synthetic conditions as in $\text{Ca}_2\text{MnTaO}_6$, which was reported to be monoclinic $P2_1/m$ (No. 11, ordered Mn and Ta at the B -sites)⁶⁵ or the competitive orthorhombic $Pbnm$ (disordering arrangement of Mn and Ta)⁶⁶ by different researchers. In our cases, all the $\text{Ca}_{2-x}\text{Mn}_x\text{MnTaO}_6$ ($0 \leq x \leq 2.0$) samples synthesized under AP and HP display black color. Both the $x = 0$ and 0.2 phases can be stabilized by chemical pressure only and synthesized under AP with a better explanation in orthorhombic $Pbnm$ from the XRD patterns (**Figure 2a**). The chemical pressure alone is not enough to stabilize the $x = 0.4$ and 0.6 samples, since impurity peaks are observed beside the target phase as shown in **Figure S1a** and **c**. Attempts to purify $x = 0.4$ and 0.6 series with additional physical pressures between 2 and 5 GPa were unsuccessful, since the impurity phases can be suppressed at higher pressure but are still distinct in XRD patterns of the 5 GPa products

(**Figure S1b** and **d**). Therefore, higher physical pressure is required to stabilize and drive pure phase with x above 0.4. **Figure 2a** clearly shows that the pure orthorhombic phase can be obtained for $0.4 \leq x \leq 1.0$ at 7 GPa. The chemical composition of selected ($x = 0.4-1.0$) specimen were confirmed by EDS analyses (**Figure S2** and **Table S1**). No single phase was achieved for x above 1.5 up to 8 GPa as shown in **Figure S1e-i**, where MnO and $\text{Mn}_3\text{Ta}_2\text{O}_8$ related phases are dominated in the $x = 2.0$ ($\text{Mn}_2\text{MnTaO}_6$) trial (**Figure S1h** and **i**). Conclusively, chemical pressure can adequately entangle Mn^{2+} at the Ca^{2+} site in $\text{Ca}_{2-x}\text{Mn}_x\text{MnTaO}_6$ for x around 0.2, and addition physical pressure of 7 GPa can assist to pump the phase boundary (x) around 1.0 (CaMnMnTaO_6) but less than 1.5 ($\text{Ca}_{0.5}\text{Mn}_{1.5}\text{MnTaO}_6$). Single phase in different structure type(s) may exist at higher pressure for $x > 1.0$ in $\text{Ca}_{2-x}\text{Mn}_x\text{MnTaO}_6$, which is, however, not the theme of this work.

The XRD peak evolution of $\text{Ca}_{2-x}\text{Mn}_x\text{MnTaO}_6$ is highlighted in the enlarged 2θ area between $21^\circ-25^\circ$ and $31^\circ-34^\circ$ in **Figure 2b**, respectively. The peaks continuously shift toward higher degree (right) with increasing x , suggesting successful incorporation of Mn^{2+} into the Ca^{2+} sites regarding their ionic radius difference. The main peak between $32-33^\circ$ is somewhat broadened in the $x = 0.6$ case compared with others, suggesting symmetry degrading or the coexistence of two phases with very similar unit cell parameters. The structure refinements were conducted for all $x = 0-1.0$ samples as shown in **Figure 3**, and the corresponding crystal structures are present in **Figure 4**. The crystal structures, besides $x = 0.6$, can be well refined in orthorhombic cell ($Pbnm$) starting from the model of $\text{La}_2\text{MgTiO}_6$.⁶⁷ The XRD patterns of $x = 0.6$ sample can be well fitted by two $Pbnm$ phases with similar cell parameters, which appeared to be x around 0.51(1) ($\text{Ca}_{1.49(1)}\text{Mn}_{0.51(1)}\text{MnTaO}_6$, 57(5)% by weight) and 0.32(1) ($\text{Ca}_{1.68(1)}\text{Mn}_{0.32(1)}\text{MnTaO}_6$, 43(7)% by weight) phases if extrapolated from the x -dependent cell

parameter evolution diagram in **Figure 5a**. In the initial structural model, sites of La and Mg/Ti ions in $\text{La}_2\text{MgTiO}_6$ were replaced by Ca/Mn and Mn/Ta ions, respectively, with fixed occupancies according to the suggested chemical formula. The refined structural parameters and the coordinates of atoms are shown in **Table 1**, and main bond lengths are listed in **Table 2**. The unit-cell dimension evolution tolerably follows Vegard's law (**Figure 5a**),⁶⁸ and the deviation may be attributed to the effect of physical pressure. The average bond lengths of (Ca1/Mn2)-O1, (Ca1/Mn2)-O2, (Ta1/Mn1)-O1, and (Ta1/Mn1)-O2 show small fluctuations (**Figure 5b**), which is unobvious to state shortened ionic bond length under chemical pressure. The bond valence sums (BVS) calculations suggest that, the *A*-site (Ca1/Mn2) is under bonded with increasing *x*, while the *B*-site (Mn1/Ta1) is over bonded. To further confirm the formal oxidation state of cations in $\text{Ca}_{2-x}\text{Mn}_x\text{MnTaO}_6$, XANES and XPS measurements were conducted for selected samples.

XANES and XPS Analyses

The Mn-K main edge of $\text{Ca}_{1.8}\text{Mn}_{0.2}\text{MnTaO}_6$ is shown in **Figure 6a** along with a series of standard spectra for comparison⁶⁹⁻⁷¹. The $\text{Sr}_2\text{Mn}^{2+}\text{ReO}_6$, and $\text{Ca}_2\text{Mn}^{3+}\text{TaO}_6$ and $\text{CaMn}^{4+}\text{O}_3$ spectra illustrate the systematic “chemical shift” of the Mn-K edge, for Mn on the perovskite *B*-site, to higher energy with increasing formal Mn-valence.⁶⁹⁻⁷¹ The $\text{Mn}^{2+}_2\text{FeReO}_6$ spectrum, on the other hand, illustrates the much lower energy onset and peak typical for Mn^{2+} on the perovskite *A*-site.^{63, 72} Close inspection of the $\text{Ca}_{1.8}\text{Mn}_{0.2}\text{MnTaO}_6$ spectrum indicates: a dominant perovskite-*B*- Mn^{3+} component based on the proximity of the main peak to that of $\text{Ca}_2\text{Mn}^{3+}\text{TaO}_6$; and a much smaller perovskite-*A*- Mn^{2+} component based on the excess spectral weight below the peak in the energy range where the $\text{Mn}^{2+}_2\text{FeReO}_6$ spectrum peaks lie. To emphasize this

difference, spectrum (Diff. Spect. in the [Figure 6a-top](#)) was calculated by first subtracting the appropriately weighted $\text{Ca}_2\text{Mn}^{3+}\text{TaO}_6$ spectrum from the $\text{Ca}_{1.8}\text{Mn}_{0.2}\text{MnTaO}_6$ spectrum and the results were normalized to the standard unity absorption across the edge. Despite the crudeness of this approximation the difference spectrum manifests a very clear spectral peak at precisely the peak energy of the perovskite-A-site standard $\text{Mn}^{2+}_2\text{FeReO}_6$. Thus, there is a strong conclusion that the Mn-K edge results support the $\sim\text{Mn}^{3+}$ (perovskite-B-site) and $\sim\text{Mn}^{2+}$ (perovskite-A-site) assignments respectively for the Mn and $\text{Mn}_{0.2}$ components in the $\text{Ca}_{1.8}\text{Mn}_{0.2}\text{MnTaO}_6$ compound formula.

The prominent bimodal A/B peak features in 5d-row $\text{L}_{2,3}$ edge features, in octahedrally coordinated oxides, have been useful probes of *d*-configuration/valence by virtue of the systematic decrease in the A (t_{2g} -hole related) feature intensity, relative to that of the B (e_g -hole related) feature. The systematic A-feature spectral weight decrease with increasing *d*-count (decreasing t_{2g} -hole count) is clearly illustrated in [Figure 6b-c](#) for standard 5d-row compounds between d^0 and d^5 .^{69, 70, 73, 74} The Ta- $\text{L}_{2,3}$ edge spectra of $\text{Ca}_{1.8}\text{Mn}_{0.2}\text{MnTaO}_6$ is plotted as a solid red line in [Figure 6b-c](#) and its large A-feature intensity very clearly supports the d^0/Ta^{5+} configuration/valence assignment for this compound. In summary the XANES results for $\text{Ca}_{1.8}\text{Mn}_{0.2}\text{MnTaO}_6$, manifest an A-site $\sim\text{Mn}^{2+}$ state, a B-site $\sim\text{Mn}^{3+}$ state, and a B'-site d^0/Ta^{5+} state.

As shown in [Figure S3](#), the XPS spectrum for Mn $2p_{3/2}$ region of CaMnMnTaO_6 ($x = 1.0$) was recorded and fitted by using XPS standard software. The spectrum exhibits three main peaks at about 640.5, 641.9, and 643.6 eV, respectively. The binding energy values are in good agreement with Mn^{2+} , Mn^{3+} , and Mn^{4+} oxidation states as reported in the literature.^{75, 76} It should be pointed out that Mn^{2+} is attributed to A-site Mn ions and Mn^{3+} corresponds to B-site Mn ions. The

appearance of Mn^{4+} could derive from charge disproportionation of Mn^{3+} into Mn^{2+} and Mn^{4+} at B -sites.^{77, 78}

Magnetic Characterization.

Figure 7 shows the temperature-dependent ZFC and FC magnetic susceptibilities (χ) for $x = 0-1.0$ samples measured at 0.1 T. In **Figure 7a**, the ferromagnetic (FM) transition temperature (T_c) can be determined as 19.6 K for $x = 0$ by means of a Curie-Weiss (CW) law fit ($\chi = C/(T - \theta)$), which implies that magnetic transition is due to spin-only Mn^{3+} ($S = 2$) and $\text{Mn}^{3+}\text{-O}^{2-}\text{-Mn}^{3+}$ superexchange interactions. As shown in **Figure 7b**, on account of the spin magnetization of Mn^{3+} at B site and the doping of Mn^{2+} at A site, two magnetic transitions appeared with $x = 0.2$. The effective magnetic moment ($\mu_{\text{eff}} = 5.37 \mu_B$) could be obtained by CW law fitting, which is close to the theoretical value ($5.57 \mu_B$) corresponding to spin-only A site Mn^{2+} (HS d^5) and B site Mn^{3+} (HS d^4) moments as evidenced by the crystal structure and XANES results. With the increasing of dopant, the samples of $x = 0.4$ and 0.6 phases display an antiferromagnetic (AFM) state as shown in **Figure 7c-d**. The substitution of Ca^{2+} ions by Mn^{2+} can be defined as the “chemical pressure”, which can be attributed to the decrease of magnetic transition temperature.^{79, 80} Their effective magnetic moment are greater than the calculated values due to magnetic interactions between Mn^{2+} and Mn^{3+} . As exhibited in **Figure 7e-f**, another interesting finding is that a negative ZFC $\chi(T)$ is observed in the $x = 0.8$ and 1.0 samples. This has been proposed in the literature that misplaced B -site cations can result in the antiphase boundary coming into being, which accompanied by a short-ranged FM coupling between Mn^{2+} and Mn^{4+} ions at B sites as evidenced by XPS results, and an AFM coupling occurs in the antiphase boundary. In the ZFC mode, the magnetic field of 0.1 T is insufficient to align all frozen clusters

and domain spins in the direction of field. By this sense, as the temperature decreases, the spin anti-parallel or tilt state is stabilized, resulting in the residual magnetization tends to be negative. A similar phenomenon occurred in $R_2\text{NiMnO}_6$ ($R = \text{Pr, Nd, Y, and Ho}$) and $\text{La}_{2-x}\text{Bi}_x\text{CoMnO}_6$ ($x = 0$ and 0.1).^{81, 82}

The isothermal magnetization $M(H)$ was measured at different temperatures from 5 to 300 K under magnetic field between -5 and 5 T. The $M(H)$ results presented in **Figure 8** support this conclusion with the magnetic hysteresis loop below $T = 10$ K, most dramatically evidencing a first-order increasing-field-induced transition out of the AFM state. Samples of $x = 0$ and 0.4 had S-type shape curves in 10 K, which reflected typical spin-glass-like magnetic properties, displayed in **Figure 8a** and **c**, respectively. The other samples showed a clear hysteresis loop given in **Figure 8b, d-f**. Their FM properties appeared with decreasing temperature owing to the concentration of induced magnetic moments on Mn at the A site increasing. The magnetic parameters of $\text{Ca}_{2-x}\text{Mn}_x\text{MnTaO}_6$ system with $0 \leq x \leq 1.0$ were summarized in **Table 4**, and have been used to map the magnetic phase diagram as shown in **Figure 9**. Samples of $x = 0$ and 0.2 were FM phases with $T_C = 19.6$ and 44 K, respectively. It can be found in $\text{Ca}_{2-x}\text{Mn}_x\text{MnTaO}_6$ for $0.4 \leq x \leq 1.0$ that Mn^{2+} at the A site involved in the long-range magnetic order and enhances the AFM order Mn-O-Mn super-exchange with increment of x , and T_N gradually becomes larger and tends to be gentle.

Unlike the other exotic perovskite with 50% of the A-site occupied by transition metal cations, such as the A-site columnar-ordered $P4_2/n$ -type quadruple perovskites CaMnBReO_6 ($B = \text{Mn},^{20} \text{Fe},^{20} \text{Co},^{21} \text{Ni}^{21}$), $\text{CaMn}_{0.5}\text{Cu}_{0.5}\text{FeReO}_6$,²⁰ and RMnMnSbO_6 ($R = \text{La, Pr, Nd, Sm}$),²² and $P4_2mc$ structural $\text{Ca}_{1.4}\text{Mn}_{0.6}\text{Ti}_2\text{O}_6$ in $\text{Ca}_{2-x}\text{Mn}_x\text{Ti}_2\text{O}_6$ ($x \leq 0.6$),¹⁹ either A- or B-site cationic ordering is absent in $\text{Ca}_{2-x}\text{Mn}_x\text{MnTaO}_6$, and the structural formula can be written as

$(\text{Ca}_{1-x/2}\text{Mn}_{x/2})(\text{Mn}_{0.5}\text{Ta}_{0.5})\text{O}_3$, namely $(\text{Ca}^{2+}_{0.5}\text{Mn}^{2+}_{0.5})(\text{Mn}^{3+}_{0.5}\text{Ta}^{5+}_{0.5})\text{O}_3$ other than CaMnMnTaO_6 for $x = 1.0$, which is, to the best of our knowledge, for the first time observed in exotic perovskite with half of the A-site occupied by small transition metal ions. In $\text{Ca}_{2-x}\text{Mn}_x\text{Ti}_2\text{O}_6$ prepared under chemical and soft physical pressure, similar A-site Ca/Mn disordering was observed for x below 0.4. However, A-site columnar-ordered quadruple perovskite $A_2A'A''B_4\text{O}_{12}$ is obtained for $\text{Ca}_{2-x}\text{Mn}_x\text{Ti}_2\text{O}_6$ with $0.4 \leq x \leq 0.6$.¹⁹ When Ti^{4+} was replaced by Mn/Ta in $\text{Ca}_{2-x}\text{Mn}_x\text{Ti}_2\text{O}_6$, the A-site columnar-ordered vanished in this work. Probably, the coexistence of B-site Mn^{3+} (Jahn-Teller distortion ion) and B'-site Ta^{5+} (second-order Jahn-Teller distortion ion) does not favor the formation of A-site columnar ordered perovskite structure $(\text{Ca})^{A_2}(\text{Mn})^{A'}(\text{Mn})^{A''}(\text{Mn})^{B_2}(\text{Ta})^{B'}\text{O}_{12}$ ($x = 1.0$ case), and the cationic disordering at both the A- and B-sites, together with charge disproportionation of Mn^{3+} into Mn^{2+} and Mn^{4+} at the B-sites, synergically renders a lower energy ground state in *Pbnm* structure in $\text{Ca}_{2-x}\text{Mn}_x\text{MnTaO}_6$.

Conclusions

In conclusion, we have prepared new exotic perovskite oxides $\text{Ca}_{2-x}\text{Mn}_x\text{MnTaO}_6$ ($0 \leq x \leq 1.0$) by means of combining chemical and physical pressure technique. The lower-Mn compounds ($x \leq 0.2$) can be solely stabilized by chemical pressure, while the target phase dominated samples can be achieved at pressure of 2-5 GPa for $0.4 \leq x \leq 0.6$ and pressure around 7 GPa at $0.8 \leq x \leq 1.0$. The crystal structure remains *Pbnm* as in $\text{Ca}_2\text{MnTaO}_6$, and can be structurally written as $(\text{Ca}_{1-x/2}\text{Mn}_{x/2})(\text{Mn}_{1/2}\text{Ta}_{1/2})\text{O}_3$ without expected A-site columnar-ordering. Both the X-ray absorption near edge and photoelectric spectroscopy data suggested $\text{Ca}_{2-x}\text{Mn}^{2+}_x\text{Mn}^{3+}\text{Ta}^{5+}\text{O}_6$ ($0 \leq x \leq 0.6$) and $\text{Ca}_{2-x}\text{Mn}^{2+}_x(\text{Mn}^{3+,2+/4+})\text{Ta}^{5+}\text{O}_6$ ($0.8 \leq x \leq 1.0$). The spin-only A site Mn^{2+} (high spin d^5) and B site Mn^{3+} (high spin d^4) moments enhance a ferromagnetic ($x \leq 0.2$) to

antiferromagnetic ($0.4 \leq x \leq 1.0$) transition around the boundary of $x = 0.2$. The partial charge disproportionation of the *B*-site Mn^{3+} into Mn^{2+} and Mn^{4+} $x = 0.8$ and 1.0 introduces negative ZFC magnetization stemming from the formation of spin antiparallel or ferromagnetic clusters and domains separating by the antiphase boundaries. This charge disproportionation over the *B*-sites could have synergically contribution to stabilize the highly disordered *Pbnm* structure in $\text{Ca}_{2-x}\text{Mn}_x\text{MnTaO}_6$. The present findings update the fundamental understanding of fixing of high-pressure phase in an ambient-pressure phase matrix, and imply that the coexistence of Jahn-Teller distorted ions at the *B*- and *B'*-sites should be avoid in $A_2A'A''B_2B'_2\text{O}_{12}$ to ensure cationic ordering and strong magnetic interactions.

ASSOCIATED CONTENT

Supporting Information

XRD patterns for unsynthesized phases; Mn 2p_{3/2} XPS binding energy; EDS spectra and analysis

Crystallographic information file for $\text{Ca}_{1.8}\text{Mn}_{0.2}\text{MnTaO}_6$ (CIF)

Crystallographic information file for $\text{Ca}_{1.6}\text{Mn}_{0.4}\text{MnTaO}_6$ (CIF)

Crystallographic information file for $\text{Ca}_{1.2}\text{Mn}_{0.8}\text{MnTaO}_6$ (CIF)

Crystallographic information file for CaMnMnTaO_6 (CIF)

AUTHOR INFORMATION

Corresponding Authors

*E-mail: limanrong@mail.sysu.edu.cn.

ORCID

Man-Rong Li: [0000-0001-8424-9134](https://orcid.org/0000-0001-8424-9134)

Yalin Ma: [0000-0002-6378-9390](https://orcid.org/0000-0002-6378-9390)

Yifeng Han: [0000-0002-7518-978X](https://orcid.org/0000-0002-7518-978X)

Notes

The authors declare no competing financial interest. The supporting crystallographic information file may also be obtained from FIZ Karlsruhe, 76344 Eggenstein-Leopoldshafen, Germany (e-mail: crysddata@fiz-karlsruhe.de), on quoting the deposition number: $x = 0.2$ (CSD1972421), $x = 0.4$ (CSD 1972420), $x = 0.8$ (CSD1972419), $x = 1.0$ (CSD 1972422).

ACKNOWLEDGMENTS

This work was financially supported by the National Science Foundation of China (NSFC-21801253, 11804404, and 21875287).

References

1. Peña, M. A.; Fierro, J. L. G., Chemical Structures and Performance of Perovskite Oxides. *Chem. Rev.* **2001**, *101* (7), 1981-2018.
2. Raveau, B., The perovskite history: More than 60 years of research from the discovery of ferroelectricity to colossal magnetoresistance via high T_C superconductivity. *Prog. Solid State Chem.* **2007**, *35* (2), 171-173.
3. Vasala, S.; Karppinen, M., A₂B'B''O₆ perovskites: A review. *Progress in Solid State Chemistry* **2015**, *43* (1-2), 1-36.
4. Serrate, D.; Teresa, J. M. D.; Ibarra, M. R., Double perovskites with ferromagnetism above room temperature. *J. Phys.: Condens. Matter* **2007**, *19* (2), 023201.
5. Goldschmidt, V. M., Die Gesetze der Krystallochemie. *Die Naturwissenschaften* **1926**, *14* (21), 477-485.
6. Li, W.; Ionescu, E.; Riedel, R.; Gurlo, A., Can we predict the formability of perovskite oxynitrides from tolerance and octahedral factors? *Journal of Materials Chemistry A* **2013**, *1* (39), 12239-12245.
7. Begiri, D.; Cascos, V.; Roberts-Watts, J.; Clark, E. R.; Bousquet, E.; Bristowe, N. C.; McCabe, E. E., Tuning octahedral tilts and the polar nature of A-site deficient perovskites. *Chem. Commun.* **2019**, *55* (18), 2609-2612.
8. Bartel, C. J.; Sutton, C.; Goldsmith, B. R.; Ouyang, R.; Musgrave, C. B.; Ghiringhelli, L. M.; Scheffler, M., New tolerance factor to predict the stability of perovskite oxides and halides. *Science Advances* **2019**, *5* (2), eaav0693.
9. Filip, M. R.; Giustino, F., The geometric blueprint of perovskites. *Proceedings of the National Academy of Sciences* **2018**, *115* (21), 5397.

10. Zhang, H.; Li, N.; Li, K.; Xue, D., Structural stability and formability of ABO_3 -type perovskite compounds. *Acta Crystallogr. Sec. B* **2007**, *63* (6), 812-818.
11. Barnes, P. W.; Lufaso, M. W.; Woodward, P. M., Structure determination of $A_2M^{3+}TaO_6$ and $A_2M^{3+}NbO_6$ ordered perovskites: octahedral tilting and pseudosymmetry. *Acta Crystallogr B* **2006**, *62* (Pt 3), 384-96.
12. Lufaso, M. W.; Woodward, P. M., Jahn-Teller distortions, cation ordering and octahedral tilting in perovskites. *Acta Crystallographica Section B* **2004**, *60* (1), 10-20.
13. Li, M.-R.; Stephens, P. W.; Croft, M.; Deng, Z.; Li, W.; Jin, C.; Retuerto, M.; Hodges, J. P.; Frank, C. E.; Wu, M.; Walker, D.; Greenblatt, M., $Mn_2(Fe_{0.8}Mo_{0.2})MoO_6$: A Double Perovskite with Multiple Transition Metal Sublattice Magnetic Effects. *Chemistry of Materials* **2018**, *30* (14), 4508-4514.
14. Li, M.-R.; Hodges, J. P.; Retuerto, M.; Deng, Z.; Stephens, P. W.; Croft, M. C.; Deng, X.; Kotliar, G.; Sánchez-Benítez, J.; Walker, D.; Greenblatt, M., Mn_2MnReO_6 : Synthesis and Magnetic Structure Determination of a New Transition-Metal-Only Double Perovskite Canted Antiferromagnet. *Chem. Mater.* **2016**, *28* (9), 3148-3158.
15. Li, M.-R.; Retuerto, M.; Deng, Z.; Stephens, P. W.; Croft, M.; Huang, Q.; Wu, H.; Deng, X.; Kotliar, G.; Sánchez-Benítez, J.; Hadermann, J.; Walker, D.; Greenblatt, M., Giant Magnetoresistance in the Half-Metallic Double-Perovskite Ferrimagnet Mn_2FeReO_6 . *Angew. Chem. Int. Ed.* **2015**, *54* (41), 12069-12073.
16. Hossain, A.; Bandyopadhyay, P.; Roy, S., An overview of double perovskites $A_2B'B''O_6$ with small ions at A site: Synthesis, structure and magnetic properties. *J. Alloys Compd.* **2018**, *740*, 414-427.
17. Leinenweber, K.; Parise, J., High-Pressure Synthesis and Crystal Structure of $CaFeTi_2O_6$, a New Perovskite Structure Type. *J. Solid State Chem.* **1995**, *114* (1), 277-281.
18. Aimi, A.; Mori, D.; Hiraki, K.-i.; Takahashi, T.; Shan, Y. J.; Shirako, Y.; Zhou, J.; Inaguma, Y., High-Pressure Synthesis of A-Site Ordered Double Perovskite $CaMnTi_2O_6$ and Ferroelectricity Driven by Coupling of A-Site Ordering and the Second-Order Jahn–Teller Effect. *Chemistry of Materials* **2014**, *26* (8), 2601-2608.
19. Li, Z.; Cho, Y.; Li, X.; Li, X.; Aimi, A.; Inaguma, Y.; Alonso, J. A.; Fernandez-Diaz, M. T.; Yan, J.; Downer, M. C.; Henkelman, G.; Goodenough, J. B.; Zhou, J., New Mechanism for Ferroelectricity in the Perovskite $Ca_{2-x}Mn_xTi_2O_6$ Synthesized by Spark Plasma Sintering. *J. Am. Chem. Soc.* **2018**.
20. McNally, G. M.; Arévalo-López, Á. M.; Kearins, P.; Orlandi, F.; Manuel, P.; Attfield, J. P., Complex Ferrimagnetism and Magnetoresistance Switching in Ca-Based Double Double and Triple Double Perovskites. *Chemistry of Materials* **2017**, *29* (20), 8870-8874.
21. Solana-Madruga, E.; Sun, Y.; Arévalo-López, Á. M.; Attfield, J. P., Ferri- and ferro-magnetism in $CaMnMReO_6$ double double perovskites of late transition metals $M = Co$ and Ni . *Chem. Commun.* **2019**, *55* (18), 2605-2608.
22. Solana-Madruga, E.; Arévalo-López, Á. M.; Dos Santos-García, A. J.; Urones-Garrote, E.; Ávila-Brandé, D.; Sáez-Puche, R.; Attfield, J. P., Double Double Cation Order in the High-Pressure Perovskites $MnRMnSbO_6$. *Angew. Chem. Int. Ed.* **2016**, *55* (32), 9340-9344.
23. Belik, A. A., Rise of A-site columnar-ordered $A_2A'A''B_4O_{12}$ quadruple perovskites with intrinsic triple order. *Dalton Trans.* **2018**, *47* (10), 3209-3217.
24. Belik, A. A.; Zhang, L.; Matsushita, Y.; Katsuya, Y.; Tanaka, M.; Yamaura, K., Crystal structures of cation non-stoichiometric RMn_3O_6 ($R = Gd, Er, \text{ and } Tm$) manganites

belonging to A-site columnar-ordered quadruple perovskite family. *Journal of Solid State Chemistry* **2019**, 275, 43-48.

25. Belik, A. A.; Khalyavin, D. D.; Zhang, L.; Matsushita, Y.; Katsuya, Y.; Tanaka, M.; Johnson, R. D.; Yamaura, K., Intrinsic Triple Order in A-site Columnar-Ordered Quadruple Perovskites: Proof of Concept. **2018**, 19 (19), 2449-2452.

26. Zhang, L.; Matsushita, Y.; Yamaura, K.; Belik, A. A., Five-Fold Ordering in High-Pressure Perovskites RMn_3O_6 ($\text{R} = \text{Gd-Tm}$ and Y). *Inorg. Chem.* **2017**, 56 (9), 5210-5218.

27. Zhang, S.; Saito, T.; Mizumaki, M.; Chen, W.-t.; Tohyama, T.; Shimakawa, Y., Site-Selective Doping Effect in $\text{AMn}_3\text{V}_4\text{O}_{12}$ ($\text{A} = \text{Na}^+$, Ca^{2+} , and La^{3+}). *J. Am. Chem. Soc.* **2012**, 135 (16), 6056-6060.

28. Long, Y. W.; Hayashi, N.; Saito, T.; Azuma, M.; Muranaka, S.; Shimakawa, Y., Temperature-induced A-B intersite charge transfer in an A-site-ordered $\text{LaCu}_3\text{Fe}_4\text{O}_{12}$ perovskite. *Nature* **2009**, 458 (7234), 60-63.

29. Ovsyannikov, S. V.; Bykova, E.; Pakhomova, A.; Kozlenko, D. P.; Bykov, M.; Kichanov, S. E.; Morozova, N. V.; Korobeinikov, I. V.; Wilhelm, F.; Rogalev, A.; Tsirlin, A. A.; Kurnosov, A. V.; Zainulin, Y. G.; Kadyrova, N. I.; Tyutyunnik, A. P.; Dubrovinsky, L., Structural and Magnetic Transitions in $\text{CaCo}_3\text{V}_4\text{O}_{12}$ Perovskite at Extreme Conditions. *Inorg. Chem.* **2017**, 56 (11), 6251-6263.

30. Ovsyannikov, S. V.; Zainulin, Y. G.; Kadyrova, N. I.; Tyutyunnik, A. P.; Semenova, A. S.; Kasinathan, D.; Tsirlin, A. A.; Miyajima, N.; Karkin, A. E., New Antiferromagnetic Perovskite $\text{CaCo}_3\text{V}_4\text{O}_{12}$ Prepared at High-Pressure and High-Temperature Conditions. *Inorg. Chem.* **2013**.

31. Shiro, K.; Yamada, I.; Ikeda, N.; Ohgushi, K.; Mizumaki, M.; Takahashi, R.; Nishiyama, N.; Inoue, T.; Irifune, T., Pd^{2+} -Incorporated Perovskite $\text{CaPd}_3\text{B}_4\text{O}_{12}$ ($\text{B} = \text{Ti}, \text{V}$). *Inorg. Chem.* **2013**, 52 (3), 1604-1609.

32. Mehmood, S.; Ali, Z.; Hashmi, Z.; Khan, S., Structural, optoelectronic and elastic properties of quaternary perovskites $\text{CaPd}_3\text{B}_4\text{O}_{12}$ ($\text{B} = \text{Ti}, \text{V}$). *Int. J. Mod Phys B* **2019**, 1950212.

33. Locherer, T.; Dinnebier, R.; Kremer, R. K.; Greenblatt, M.; Jansen, M., Synthesis and properties of a new quadruple perovskite: A-site ordered $\text{PbMn}_3\text{Mn}_4\text{O}_{12}$. *J. Solid State Chem.* **2012**, 190, 277-284.

34. Mezzadri, F.; Calicchio, M.; Gilioli, E.; Cabassi, R.; Bolzoni, F.; Calestani, G.; Bissoli, F., High-pressure synthesis and characterization of $\text{PrMn}_7\text{O}_{12}$ polymorphs. *Phys. Rev. B* **2009**, 79 (1), 014420.

35. Przeniosła, R.; Sosnowska, I.; Suard, E.; Hewat, A.; Fitch, A. N., Charge ordering and anisotropic thermal expansion of the manganese perovskite $\text{CaMn}_7\text{O}_{12}$. *Physica B: Condensed Matter* **2004**, 344 (1-4), 358-367.

36. Chen, W.-t.; Mizumaki, M.; Seki, H.; Senn, M. S.; Saito, T.; Kan, D.; Attfield, J. P.; Shimakawa, Y., A half-metallic A- and B-site-ordered quadruple perovskite oxide $\text{CaCu}_3\text{Fe}_2\text{Re}_2\text{O}_{12}$ with large magnetization and a high transition temperature. *Nat Commun* **2014**, 5.

37. Senn, M. S.; Chen, W.-t.; Saito, T.; García-Martín, S.; Attfield, J. P.; Shimakawa, Y., B-Cation Order Control of Magnetism in the 1322 Perovskite $\text{CaCu}_3\text{Fe}_2\text{Nb}_2\text{O}_{12}$. *Chem. Mater.* **2014**, 26 (16), 4832-4837.

38. Wang, X.; Liu, M.; Shen, X.; Liu, Z.; Hu, Z.; Chen, K.; Ohresser, P.; Nataf, L.; Baudalet, F.; Lin, H.-J.; Chen, C.-T.; Soo, Y.-L.; Yang, Y.-f.; Jin, C.; Long, Y.,

High-Temperature Ferrimagnetic Half Metallicity with Wide Spin-up Energy Gap in $\text{NaCu}_3\text{Fe}_2\text{Os}_2\text{O}_{12}$. *Inorg. Chem.* **2019**, 58 (1), 320-326.

39. Prodi, A.; Gilioli, E.; Cabassi, R.; Bolzoni, F.; Licci, F.; Huang, Q.; Lynn, J. W.; Affronte, M.; Gauzzi, A.; Marezio, M., Magnetic structure of the high-density single-valent e_g Jahn-Teller system $\text{LaMn}_7\text{O}_{12}$. *Phys. Rev. B* **2009**, 79 (8), 085105.

40. Mezzadri, F.; Calestani, G.; Calicchio, M.; Gilioli, E.; Bolzoni, F.; Cabassi, R.; Marezio, M.; Migliori, A., Synthesis and characterization of multiferroic $\text{BiMn}_7\text{O}_{12}$. *Phys. Rev. B* **2009**, 79 (10), 100106.

41. Belik, A. A.; Matsushita, Y.; Kumagai, Y.; Katsuya, Y.; Tanaka, M.; Stefanovich, S. Y.; Lazoryak, B. I.; Oba, F.; Yamaura, K., Complex Structural Behavior of $\text{BiMn}_7\text{O}_{12}$ Quadruple Perovskite. *Inorg. Chem.* **2017**, 56 (20), 12272-12281.

42. Kawamoto, T.; Fujita, K.; Yamada, I.; Matoba, T.; Kim, S. J.; Gao, P.; Pan, X.; Findlay, S. D.; Tassel, C.; Kageyama, H.; Studer, A. J.; Hester, J.; Irifune, T.; Akamatsu, H.; Tanaka, K., Room-Temperature Polar Ferromagnet ScFeO_3 Transformed from a High-Pressure Orthorhombic Perovskite Phase. *J. Am. Chem. Soc.* **2014**, 136 (43), 15291-15299.

43. Liu, L.; Song, H. X.; Li, X.; Zhang, D.; Mathieu, R.; Ivanov, S.; Skogby, H.; Lazor, P., Pressure-induced polymorphism and piezochromism in $\text{Mn}_2\text{FeSbO}_6$. *Appl. Phys. Lett.* **2019**, 114 (16), 162903.

44. Su, H.-P.; Li, S.-F.; Han, Y.; Wu, M.-X.; Gui, C.; Chang, Y.; Croft, M.; Ehrlich, S.; Khalid, S.; Adem, U.; Dong, S.; Sun, Y.; Huang, F.; Li, M.-R., Predicted polymorph manipulation in an exotic double perovskite oxide. *Journal of Materials Chemistry C* **2019**, 7 (39), 12306-12311.

45. Markkula, M.; Arevalo-Lopez, A. M.; Kusmartseva, A.; Rodgers, J. A.; Ritter, C.; Wu, H.; Attfield, J. P., Incommensurate spin order in the metallic perovskite MnVO_3 . *Phys. Rev. B* **2011**, 84 (9), 094450.

46. Belik, A. A.; Matsushita, Y.; Tanaka, M.; Takayama-Muromachi, E., Crystal Structures and Properties of Perovskites ScCrO_3 and InCrO_3 with Small Ions at the A Site. *Chem. Mater.* **2012**, 24 (11), 2197-2203.

47. Alexei, A. B.; Wei, Y., High-pressure synthesis, crystal chemistry and physics of perovskites with small cations at the A site. *J. Phys.: Condens. Matter* **2014**, 26 (16), 163201.

48. Solana-Madruga, E.; Dos santos-Garcia, A. J.; Arevalo-Lopez, A. M.; Avila-Brandé, D.; Ritter, C.; Attfield, J. P.; Saez-Puche, R., High pressure synthesis of polar and non-polar cation-ordered polymorphs of $\text{Mn}_2\text{ScSbO}_6$. *Dalton Transactions* **2015**, 44 (47), 20441-20448.

49. Bazuev, G. V.; Tyutyunnik, A. P.; Kuznetsov, M. V.; Zainulin, Y. G., Structural, Magnetic, and XPS Studies of the Double-Perovskite Mn_2VSbO_6 . *Journal of Superconductivity and Novel Magnetism* **2018**.

50. Arevalo-Lopez, A. M.; Stegemann, F.; Attfield, J. P., Competing antiferromagnetic orders in the double perovskite $\text{Mn}_2\text{MnReO}_6$ (Mn_3ReO_6). *Chem. Commun.* **2016**, 52 (32), 5558-5560.

51. Arévalo-López, A. M.; McNally, G. M.; Attfield, J. P., Large Magnetization and Frustration Switching of Magnetoresistance in the Double-Perovskite Ferrimagnet $\text{Mn}_2\text{FeReO}_6$. *Angew. Chem. Int. Ed.* **2015**, 54 (41), 12074-12077.

52. Frank, C. E.; McCabe, E. E.; Orlandi, F.; Manuel, P.; Tan, X.; Deng, Z.; Croft, M.; Cascos, V.; Emge, T.; Feng, H. L.; Lapidus, S.; Jin, C.; Wu, M.; Li, M. R.; Ehrlich, S.; Khalid, S.; Quackenbush, N.; Yu, S.; Walker, D.; Greenblatt, M., $\text{Mn}_2\text{CoReO}_6$: a robust multisublattice antiferromagnetic perovskite with small A-site cations. *Chem. Commun.* **2019**, 55 (23), 3331-3334.

53. Akizuki, Y.; Yamada, I.; Fujita, K.; Taga, K.; Kawakami, T.; Mizumaki, M.; Tanaka, K., Rattling in the Quadruple Perovskite $\text{CuCu}_3\text{V}_4\text{O}_{12}$. *Angew. Chem. Int. Ed.* **2015**, *54* (37), 10870-10874.
54. Akizuki, Y.; Yamada, I.; Fujita, K.; Nishiyama, N.; Irifune, T.; Yajima, T.; Kageyama, H.; Tanaka, K., A-Site-Ordered Perovskite $\text{MnCu}_3\text{V}_4\text{O}_{12}$ with a 12-Coordinated Manganese(II). *Inorg. Chem.* **2013**, *52* (19), 11538-11543.
55. Ovsyannikov, S. V.; Abakumov, A. M.; Tsirlin, A. A.; Schnelle, W.; Egoavil, R.; Verbeeck, J.; Van Tendeloo, G.; Glazyrin, K. V.; Hanfland, M.; Dubrovinsky, L., Perovskite-like Mn_2O_3 : a path to new manganites. *Angew. Chem. Int. Ed.* **2013**, *52* (5), 1494-8.
56. Murakami, M.; Hirose, K.; Kawamura, K.; Sata, N.; Ohishi, Y., Post-Perovskite Phase Transition in MgSiO_3 . *Science* **2004**, *304* (5672), 855-858.
57. Santillán, J.; Shim, S.-H.; Shen, G.; Prakapenka, V. B., High-pressure phase transition in Mn_2O_3 : Application for the crystal structure and preferred orientation of the CaIrO_3 type. *Geophys. Res. Lett.* **2006**, *33* (15), n/a-n/a.
58. Ruiz-Fuertes, J.; Bernert, T.; Zimmer, D.; Schrod, N.; Koch-Müller, M.; Winkler, B.; Bayarjargal, L.; Popescu, C.; MacLeod, S.; Glazyrin, K., Ambient-temperature high-pressure-induced ferroelectric phase transition in $\text{CaMnTi}_2\text{O}_6$. *Phys. Rev. B* **2017**, *96* (9), 094101.
59. Gou, G.; Charles, N.; Shi, J.; Rondinelli, J. M., A-Site Ordered Double Perovskite $\text{CaMnTi}_2\text{O}_6$ as a Multifunctional Piezoelectric and Ferroelectric–Photovoltaic Material. *Inorg. Chem.* **2017**, *56* (19), 11854-11861.
60. Li, J.; Lorger, S.; Stalick, J. K.; Sleight, A. W.; Subramanian, M. A., From Serendipity to Rational Design: Tuning the Blue Trigonal Bipyramidal Mn^{3+} Chromophore to Violet and Purple through Application of Chemical Pressure. *Inorg. Chem.* **2016**, *55* (19), 9798-9804.
61. Shannon, R., Revised effective ionic radii and systematic studies of interatomic distances in halides and chalcogenides. *Acta Crystallogr. Sect. A* **1976**, *32* (5), 751-767.
62. Bruker AXS TOPAS V4: General profile and structure analysis software for powder diffraction data. – User’s Manual. *Bruker AXS, Karlsruhe, Germany* **2008**.
63. Wang, J.; Wylie-van Eerd, B.; Sluka, T.; Sandu, C.; Cantoni, M.; Wei, X.-K.; Kvasov, A.; McGilly, L. J.; Gemeiner, P.; Dkhil, B.; Tagantsev, A.; Trodahl, J.; Setter, N., Negative-pressure-induced enhancement in a freestanding ferroelectric. *Nat. Mater.* **2015**, *14* (10), 985-990.
64. Ali, S.; Khan, W.; Murtaza, G.; Yaseen, M.; Ramay, S. M.; Mahmood, A., First principles study of magnetic and electronic properties of $\text{A}_2\text{BB}'\text{O}_6$ ($\text{A} = \text{Ba}, \text{Sr}$) ($\text{BB}' = \text{FeRe}, \text{MnMo}, \text{and MnRe}$) double perovskites. *Journal of Magnetism and Magnetic Materials* **2017**, *441*, 113-123.
65. Mandal, T. K.; Poltavets, V. V.; Croft, M.; Greenblatt, M., Synthesis, structure and magnetic properties of $\text{A}_2\text{MnB}'\text{O}_6$ ($\text{A} = \text{Ca}, \text{Sr}$; $\text{B}' = \text{Sb}, \text{Ta}$) double perovskites. *J. Solid State Chem.* **2008**, *181* (9), 2325-2331.
66. Barnes, P. W.; Lufaso, M. W.; Woodward, P. M., Structure determination of $\text{A}_2\text{M}^{3+}\text{TaO}_6$ and $\text{A}_2\text{M}^{3+}\text{NbO}_6$ ordered perovskites: octahedral tilting and pseudosymmetry. *Acta Crystallogr. Sect. B* **2006**, *62* (3), 384-396.
67. Seabra, M. P.; Avdeev, M.; Ferreira, V. M.; Pullar, R. C.; Alford, N. M., Structure and microwave dielectric properties of $\text{La}(\text{Mg}_{0.5}\text{Ti}_{0.5})\text{O}_3\text{--CaTiO}_3$ system. *Journal of the European Ceramic Society* **2003**, *23* (14), 2403-2408.
68. Denton, A. R.; Ashcroft, N. W., Vegard's law. *Phys. Rev. A* **1991**, *43* (6), 3161-3164.

69. Popov, G.; Greenblatt, M.; Croft, M., Large effects of A-site average cation size on the properties of the double perovskites $\text{Ba}_{2-x}\text{Sr}_x\text{MnReO}_6$: A d^5-d^1 system. *Physical Review B* **2003**, 67 (2).
70. Mandal, T. K.; Poltavets, V. V.; Croft, M.; Greenblatt, M., Synthesis, structure and magnetic properties of $\text{A}_2\text{MnB}'\text{O}_6$ ($\text{A} = \text{Ca}, \text{Sr}$; $\text{B}' = \text{Sb}, \text{Ta}$) double perovskites. *Journal of Solid State Chemistry* **2008**, 181 (9), 2325-2331.
71. Bridges, F.; Booth, C. H.; Kwei, G. H.; Neumeier, J. J.; Sawatzky, G. A., Temperature dependent changes of the Mn 3d and 4p bands near T_c in colossal magnetoresistance systems: XANES study of $\text{La}_{1-x}\text{Ca}_x\text{MnO}_3$. *Physical Review B* **2000**, 61 (14).
72. Zhong, K.; Zhang, B.; Luo, S.; Wen, W.; Li, H.; Huang, X.; Chen, L., Investigation on porous MnO microsphere anode for lithium ion batteries. *Journal of Power Sources* **2011**, 196 (16), 6802-6808.
73. Retuerto, M.; Li, M.-R.; Stephens, P. W.; Sánchez-Benítez, J.; Deng, X.; Kotliar, G.; Croft, M. C.; Ignatov, A.; Walker, D.; Greenblatt, M., Half-Metallicity in $\text{Pb}_2\text{CoReO}_6$ Double Perovskite and High Magnetic Ordering Temperature in $\text{Pb}_2\text{CrReO}_6$ Perovskite. *Chemistry of Materials* **2015**, 27 (12), 4450-4458.
74. Laguna-Marco, M. A.; Kayser, P.; Alonso, J. A.; Martínez-Lope, M. J.; van Veenendaal, M.; Choi, Y.; Haskel, D., Electronic structure, local magnetism, and spin-orbit effects of Ir(IV)-, Ir(V)-, and Ir(VI)-based compounds. *Physical Review B* **2015**, 91 (21).
75. Huang, Z.; Zhou, W.; Ouyang, C.; Wu, J.; Zhang, F.; Huang, J.; Gao, Y.; Chu, J., High performance of Mn-Co-Ni-O spinel nanofilms sputtered from acetate precursors. *Sci Rep* **2015**, 5, 10899.
76. Barai, H. R.; Banerjee, A. N.; Joo, S. W., Improved electrochemical properties of highly porous amorphous manganese oxide nanoparticles with crystalline edges for superior supercapacitors. *Journal of Industrial and Engineering Chemistry* **2017**, 56, 212-224.
77. Yonemura, M.; Kohigashi, T.; Yamada, A.; Sonoyama, N.; Kobayashi, H.; Kamiyama, T.; Kanno, R., Defect structure of LiMn_2O_4 after high-temperature storage. *Electrochemistry* **2003**, 71 (12), 1160-1161.
78. Pollert, E., Influence of Mn^{3+} ions on ordering in magnetic oxides. *Int J Inorg Mater* **2000**, 2 (6), 661-670.
79. Belik, A. A.; Matsushita, Y.; Tanaka, M.; Takayama-Muromachi, E., $(\text{In}_{1-y}\text{Mn}_y)\text{MnO}_3$ ($1/9 \leq y \leq 1/3$): unusual perovskites with unusual properties. *Angewandte Chemie* **2010**, 49 (42), 7723-7.
80. Hauser, A.; Amstutz, N.; Delahaye, S.; Sadki, A.; Schenker, S.; Sieber, R.; Zerara, M., Chemical Pressure. *CHIMIA International Journal for Chemistry* **2002**, 56 (12), 685-689.
81. Nasir, M.; Kumar, S.; Patra, N.; Bhattacharya, D.; Jha, S. N.; Basaula, D. R.; Bhatt, S.; Khan, M.; Liu, S.-W.; Biring, S.; Sen, S., Role of Antisite Disorder, Rare-Earth Size, and Superexchange Angle on Band Gap, Curie Temperature, and Magnetization of R_2NiMnO_6 Double Perovskites. *ACS Applied Electronic Materials* **2019**, 1 (1), 141-153.
82. Bai, Y.; Xia, Y.; Li, H.; Han, L.; Wang, Z.; Wu, X.; Lv, S.; Liu, X.; Meng, J., A-Site-Doping Enhanced B-Site Ordering and Correlated Magnetic Property in $\text{La}_{2-x}\text{Bi}_x\text{CoMnO}_6$. *The Journal of Physical Chemistry C* **2012**, 116 (32), 16841-16847.

Figures and Captions

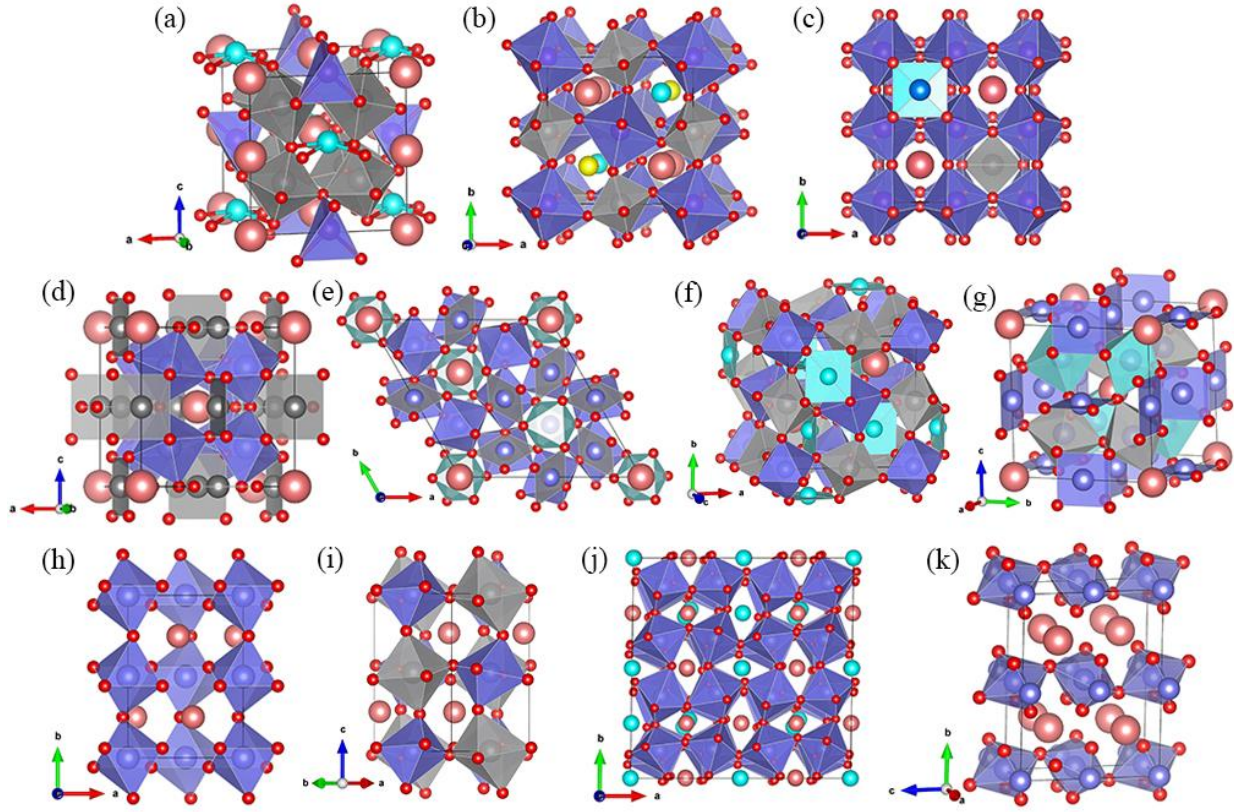


Figure 1. Crystal structures of exotic perovskite oxides with small A-site cations. A, pink spheres; O, red spheres; BO_6 octahedra, violet; $B'O_6$ octahedra, silver gray. $A_2A'A''B_4O_{12}$ with 50% of the small cationic A-sites (A' and A''): (a) A-site columnar-ordered quadruple perovskites $A_2A'A''B_4O_{12}$ (tetragonal, $P4_2mc$). $A'O_4$ square-planar, cyan; $A''O_4$ tetrahedral, violet; BO_6 octahedra, silver gray. (b) Rock-salt B-sites ordering in $A_2A'A''B_2B'_2O_{12}$ (tetragonal, $P4_2/n$). A' , cyan spheres; A'' , yellow spheres. (c) RMn_3O_6 with layered charge ordering over the B-sites (orthorhombic, $Pmmn$). $Mn1O_4$ square-planar, cyan; $Mn2O_4$ tetrahedral, silver gray; MnO_6 octahedra, violet. $AA'B_4O_{12}$ with 75% of small cationic A-sites (A'): (d) Most known $AA'B_4O_{12}$ quadruple perovskites (cubic, $Im-3$). $A'O_4$ square-planar, silver gray. (e) B-site charge-ordering of $A^{2+}Mn_3Mn_4O_{12}$ (rhombohedral, $R-3$). $Mn1O_4$ square-planar, silver gray; $Mn2O_6$ octahedra, violet; $Mn3O_6$ octahedra, cyan. (f) 1322-type B-site ordering of $AA'B_2B'_2O_{12}$ (cubic, $Pn-3$). $A'O_4$ square-planar, cyan. (g) Trivalent A-site driving Jahn-Teller distorted Mn^{3+} component on the B-site of $A^{3+}Mn_7O_{12}$ (monoclinic, $I2/m$), MnO_4 square-planar, violet; $Mn4O_6$ octahedra, silver gray; $Mn5O_6$ octahedra, cyan. Exotic perovskite with 100% of small cationic A-sites: (h) $GdFeO_3$ -based ABO_3 -type (orthorhombic, $Pnma$); (i) $A_2BB'O_6$ -type (monoclinic, $P2_1/n$), (j) ζ - Mn_2O_3 -type (triclinic, $F-1$), and (k) Post-perovskite (orthorhombic, $Cmcm$).

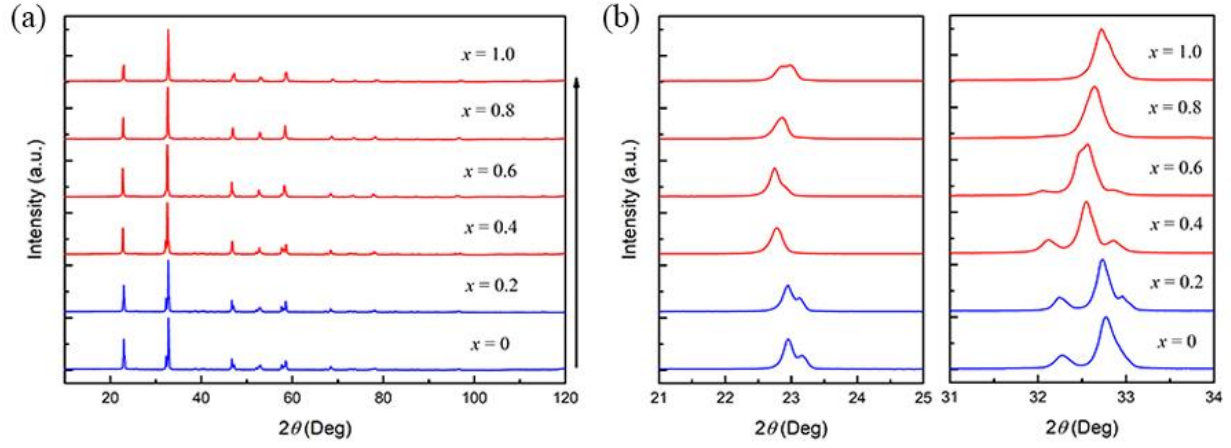


Figure 2. (a) XRD patterns of $\text{Ca}_{2-x}\text{Mn}_x\text{MnTaO}_6$ with $x = 0, 0.2, 0.4, 0.6, 0.8$ and 1.0 , where blue and red lines denote the phase prepared at AP and HP, respectively. (b) The enlarged XRD patterns between 21° - 25° (left) and 31° - 34° (right) ranges.

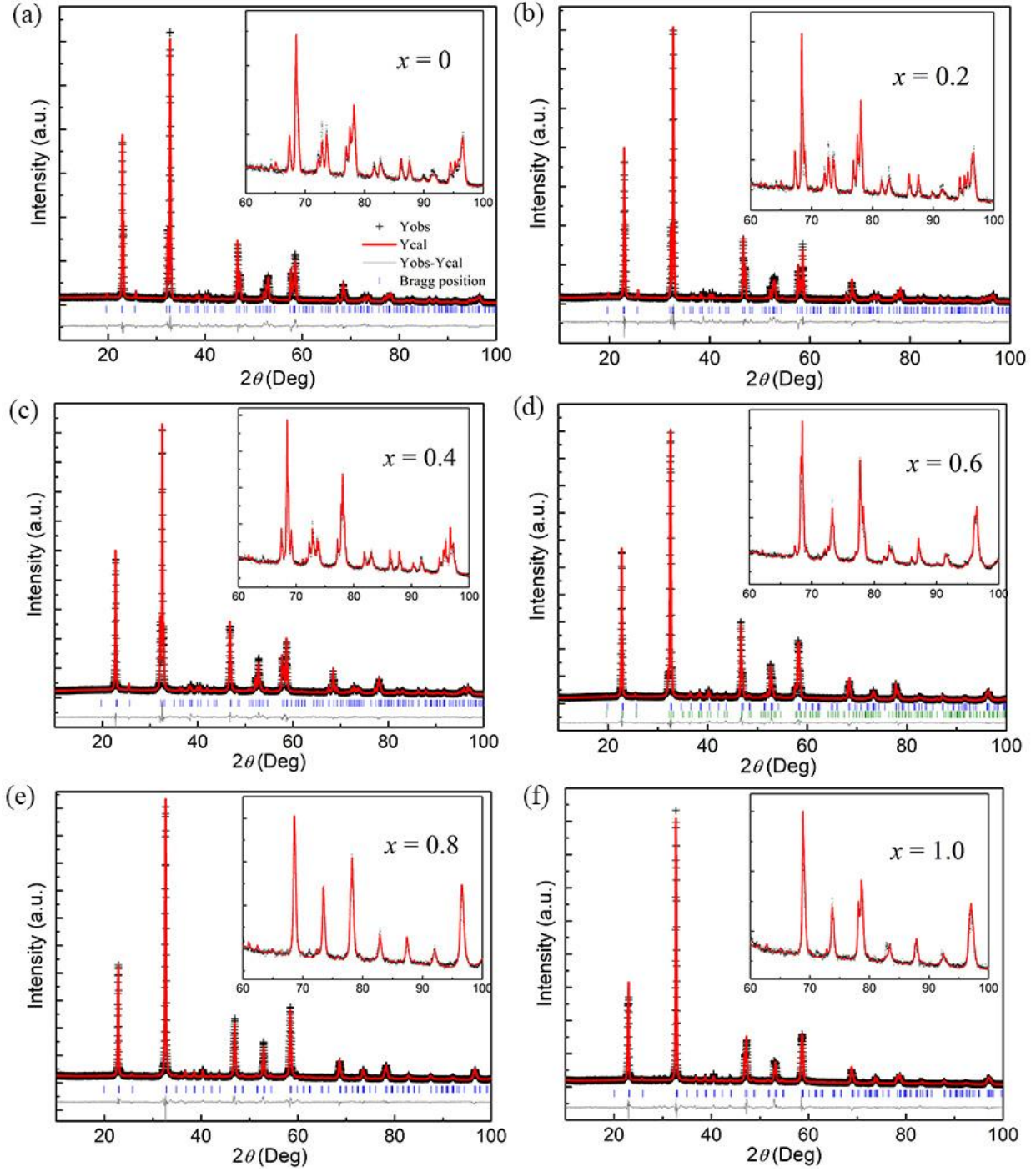


Figure 3. Rietveld refinement of XRD patterns of $\text{Ca}_{2-x}\text{Mn}_x\text{MnTaO}_6$: (a) $x = 0$; (b) $x = 0.2$; (c) $x = 0.4$; (d) $x = 0.6$; (e) $x = 0.8$; (f) $x = 1.0$. The insets ($60\text{--}100^\circ$) show enlarged views.

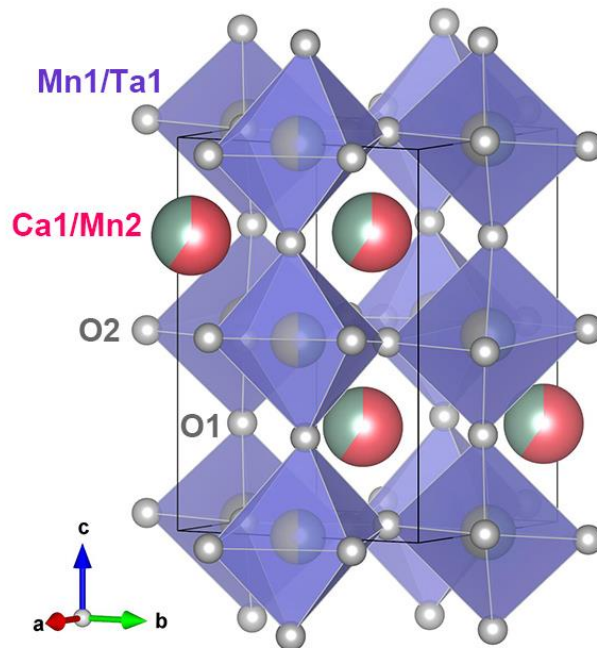


Figure 4. Crystal structure of $\text{Ca}_{2-x}\text{Mn}_x\text{MnTaO}_6$. Ca1/Mn2 are located at the A site and Mn1/Ta1 are disordered over the B site, the violet octahedra are $(\text{Mn1}, \text{Ta})\text{O}_6$.

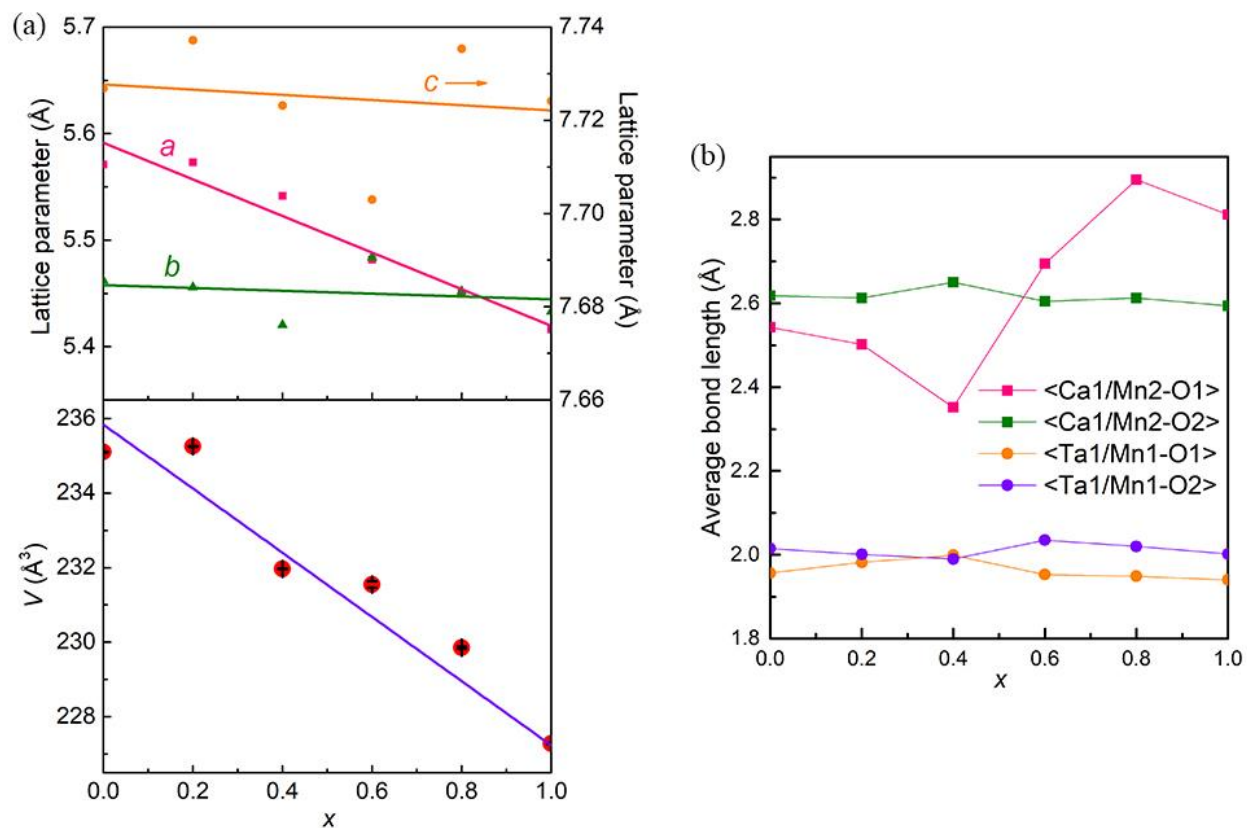


Figure 5. Mn²⁺ ion concentration dependence of (a) the orthorhombic lattice parameter a (Å), b (Å), c (Å), the unit cell volume V (Å³), and (b) average bond lengths in $\text{Ca}_{2-x}\text{Mn}_x\text{MnTaO}_6$ refined from XRD data.

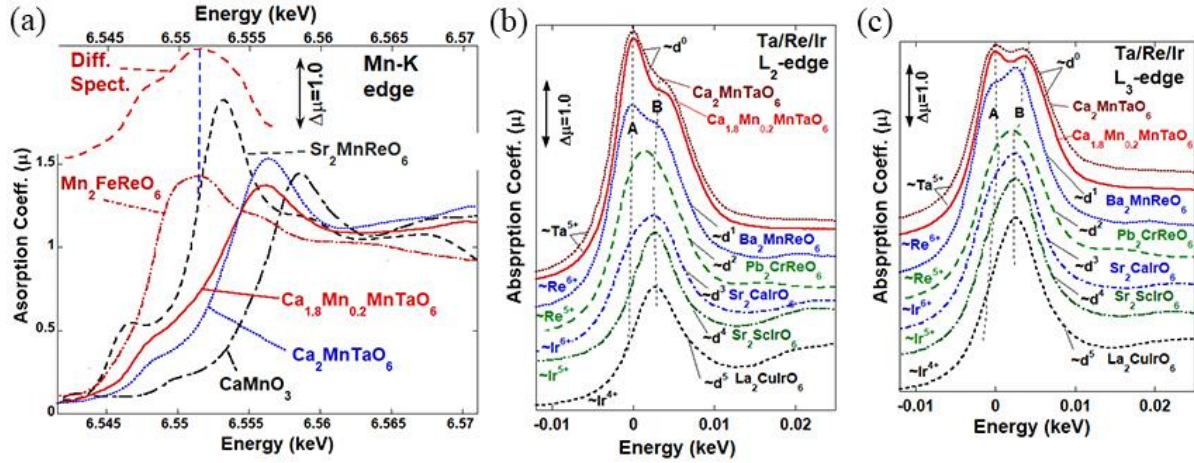


Figure 6. (a) The Mn-K edge spectra for $\text{Ca}_{1.8}\text{Mn}_{0.2}\text{MnTaO}_6$, compared with those of a series of standard compound spectra: the A-site perovskite based $\text{Mn}^{2+}\text{FeReO}_6$; the B-site perovskite based $\text{Sr}_2\text{Mn}^{2+}\text{ReO}_6$, $\text{Ca}_2\text{Mn}^{3+}\text{TaO}_6$ and $\text{CaMn}^{4+}\text{O}_3$. The spectrum labeled as “Diff. Spect.” is a weighted difference spectrum (with normalization) to estimate the A site Mn spectrum in $\text{Ca}_{1.8}\text{Mn}_{0.2}\text{MnTaO}_6$. (b) A superimposed comparison of the Ta- L_2 and L_3 edge of $\text{Ca}_{1.8}\text{Mn}_{0.2}\text{MnTaO}_6$ to those of the d^0/Ta^{5+} - $\text{Ca}_2\text{MnTaO}_6$, d^1/Re^{6+} - $\text{Ba}_2\text{MnReO}_6$, d^2/Re^{5+} - $\text{Pb}_2\text{CrReO}_6$, d^3/Ir^{6+} - $\text{Sr}_2\text{CaIrO}_6$, d^4/Ir^{5+} - $\text{Sr}_2\text{ScIrO}_6$ and d^5/Ir^{4+} - $\text{La}_2\text{CuIrO}_6$ standards, indicating Ta^{5+} in $\text{Ca}_{1.8}\text{Mn}_{0.2}\text{MnTaO}_6$.

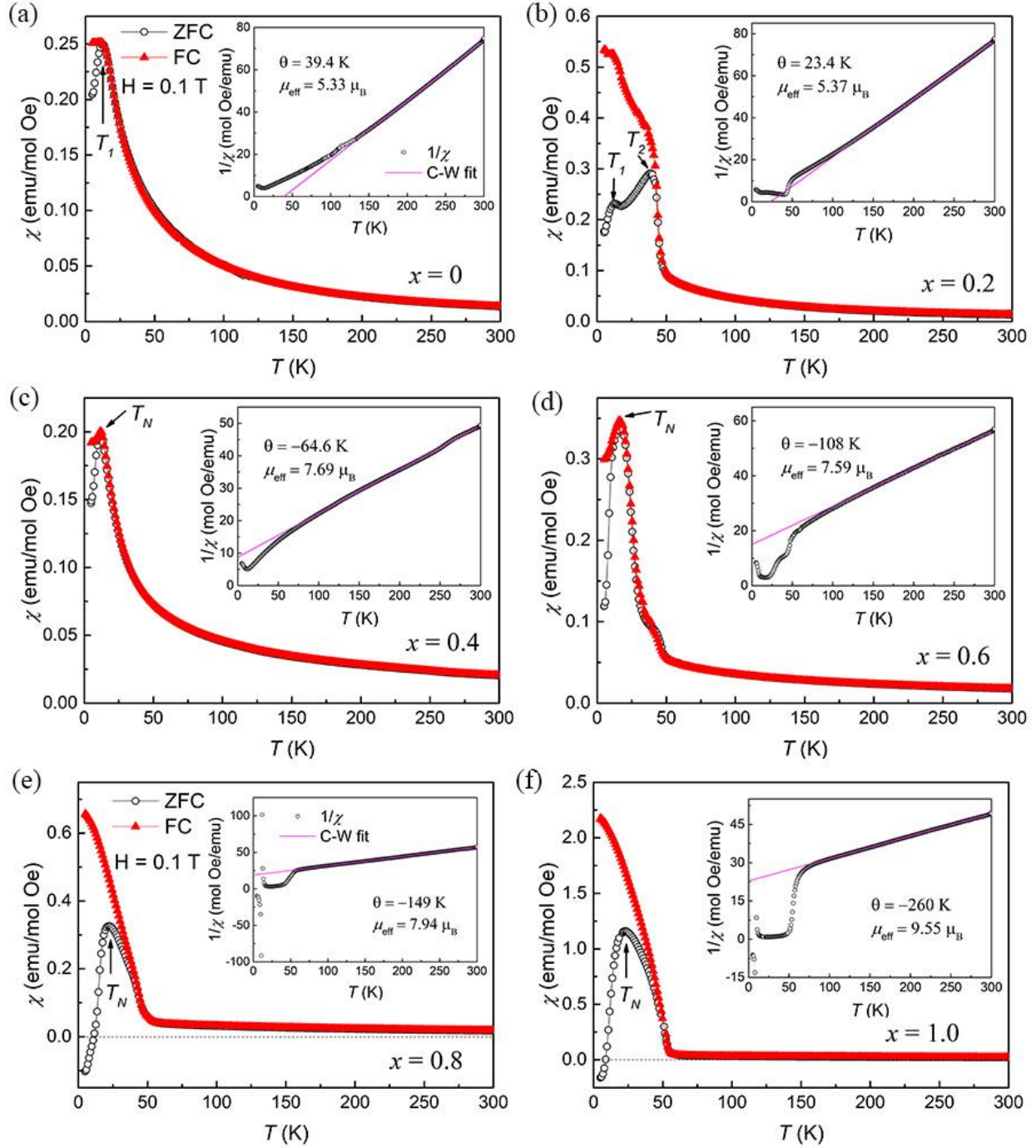


Figure 7. Magnetic properties of $\text{Ca}_{2-x}\text{Mn}_x\text{MnTaO}_6$. Temperature dependence of the magnetic susceptibilities measured at 0.1 T under zero-field-cooled (ZFC, empty circles) and field-cooled (FC, filled triangles) conditions between 5 and 300 K. (a) $x = 0$; (b) $x = 0.2$; (c) $x = 0.4$; (d) $x = 0.6$; (e) $x = 0.8$; (f) $x = 1$. The insets show the ZFC χ^{-1} vs T curves at 0.1 T with the Curie–Weiss fits.

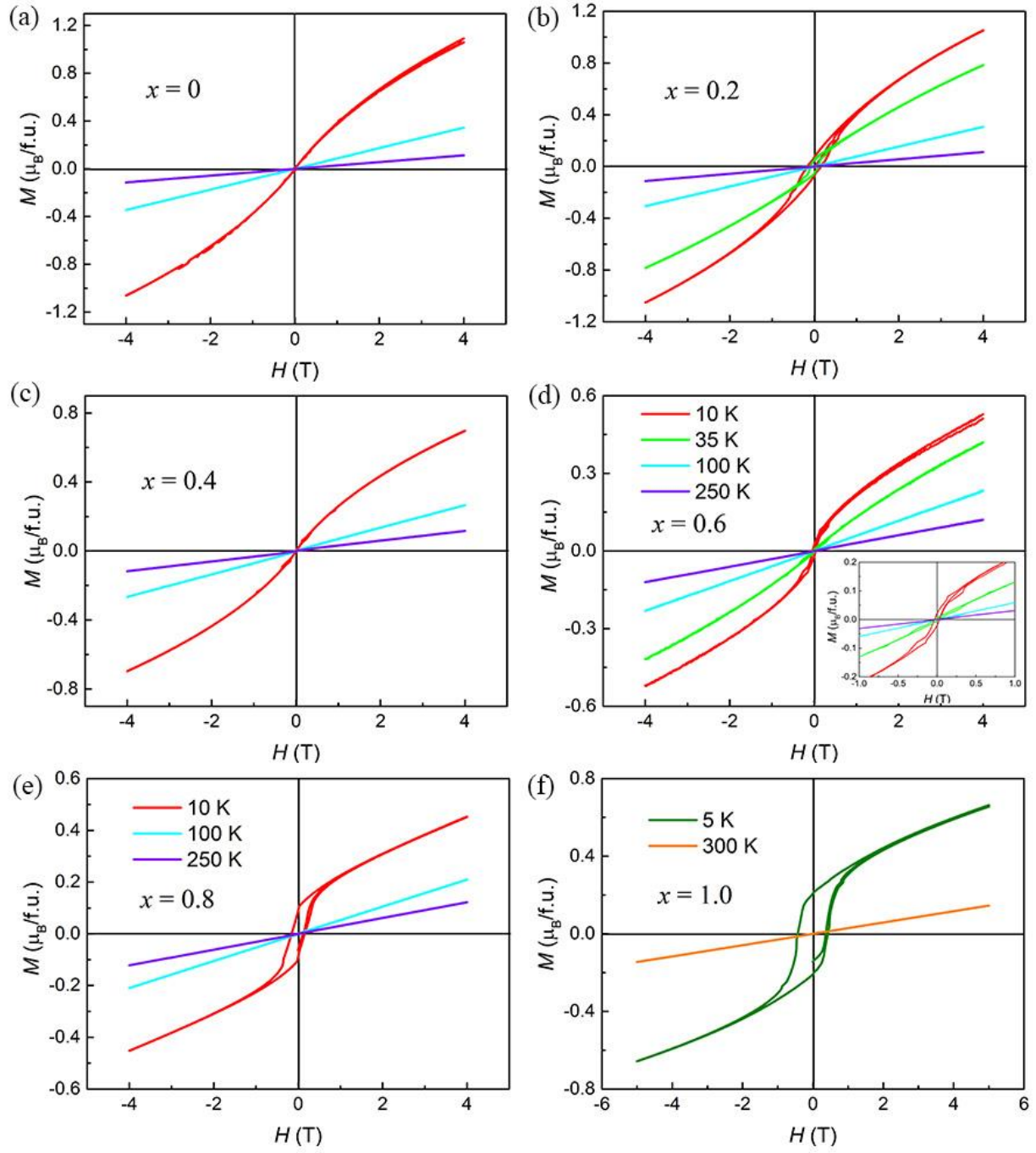


Figure 8. Isothermal magnetization curves of $\text{Ca}_{2-x}\text{Mn}_x\text{MnTaO}_6$ at 10, 35, 100, and 250 K between -4 and 4 T. (a) $x = 0$; (b) $x = 0.2$; (c) $x = 0.4$; (d) $x = 0.6$; (e) $x = 0.8$; (f) $x = 1$. The inset in (d) shows the expanded region between -1.0 and 1.0 T, showing clear hysteresis loops at different temperatures.

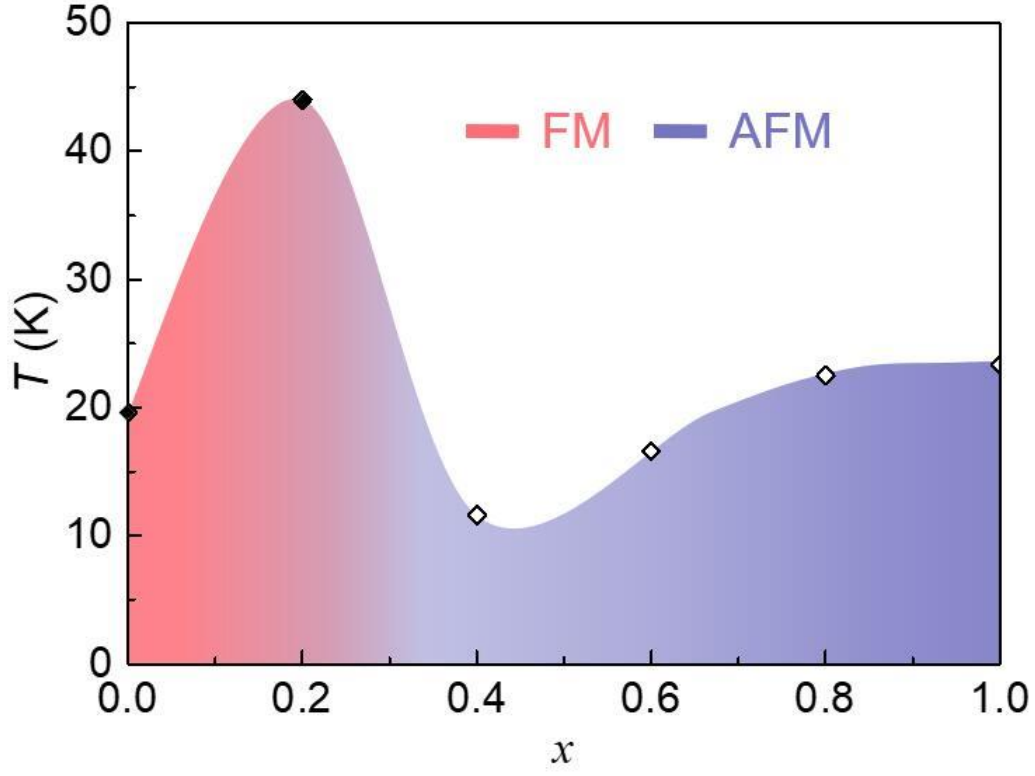


Figure 9. Magnetic phase diagram of $\text{Ca}_{2-x}\text{Mn}_x\text{MnTaO}_6$. The symbols are transition temperatures of $\text{Ca}_{2-x}\text{Mn}_x\text{MnTaO}_6$ (filled diamonds for T_C $0 \leq x \leq 0.2$, open diamonds for T_N of $0.4 \leq x \leq 1.0$). Pink area is for ferromagnetic (FM) phase, blue area for antiferromagnetic (AFM) phase.

Tables and Captions

Table 1. Structure refinements results of fractional atomic coordinates, occupancies and isotropic displacement parameters (\AA^2) of $\text{Ca}_{2-x}\text{Mn}_x\text{MnTaO}_6$ with $x = 0, 0.2, 0.4, 0.6, 0.8$ and 1.0

	$x = 0$	$x = 0.2$	$x = 0.4$	$x = 0.6$	$x = 0.8$	$x = 1.0$
				$x = 0.51$	$x = 0.32$	
$a/\text{\AA}$	5.5707 (2)	5.5731 (1)	5.5414 (1)	5.4816 (5)	5.5512 (2)	5.4160 (2)
$b/\text{\AA}$	5.4620 (2)	5.4558 (1)	5.4203 (1)	5.4838 (5)	5.4197 (3)	5.4330 (3)
$c/\text{\AA}$	7.7268 (2)	7.7371 (2)	7.7231 (2)	7.7030 (2)	7.7478 (5)	7.7241 (3)
$V/\text{\AA}^3$	235.10 (1)	235.25 (1)	231.966 (8)	231.55 (3)	233.10 (2)	227.28 (2)
Ca1/Mn2 4c (x, y, 1/4)						
x	-0.0166 (8)	-0.0262 (8)	-0.0409 (5)	-0.0327 (8)	-0.0377 (13)	0.0325 (10)
y	0.0316 (8)	0.0227 (12)	0.0247 (7)	-0.0248 (13)	0.0489 (12)	-0.0357 (8)
$Occ.$	1	0.9/0.1	0.8/0.2	0.75/0.25	0.84/0.16	0.6/0.4
B_{iso}	2.00 (15)	2.00 (16)	2.0 (2)	2.0 (2)	2.0 (9)	2.0 (3)
Mn1/Ta1 4a (1/2, 0, 0)						
B_{iso}	2.44 (14)	2.21 (15)	2.1 (2)	2.5 (2)	2.1 (8)	2.7 (3)
O1 4c (x, y, 1/4)						
x	0.0525 (18)	0.050 (2)	0.001 (3)	0.051 (4)	0.024 (6)	-0.044 (6)
y	0.481 (3)	0.439 (3)	0.4048 (16)	0.470 (6)	0.469 (4)	0.505 (3)
B_{iso}	4.0 (4)	4.0 (5)	4.0 (4)	4.0 (6)	4.0 (11)	3.5 (7)
O2 8d (x, y, z)						
x	0.7965 (15)	0.7971 (17)	0.7966 (11)	0.683 (4)	0.794 (3)	0.832 (6)
y	0.212 (2)	0.210 (2)	0.2120 (14)	0.302 (5)	0.198 (3)	0.180 (7)
z	0.0496 (8)	0.0385 (13)	-0.0397 (9)	-0.0505 (13)	-0.015 (4)	0.0177 (19)
B_{iso}	1.9 (4)	2.6 (4)	1.9 (3)	3.0 (4)	1.5 (11)	2.1 (4)
R_{wp} (%)	7.93	8.96	5.77		5.42	6.69
R_p (%)	5.77	6.53	4.25		4.06	4.84
χ^2	2.35	2.72	2.25		2.12	2.54
R_B (%)	4.13	4.81	2.72	2.87	2.33	2.64

Table 2. Selected bond lengths (Å) and BVS of $\text{Ca}_{2-x}\text{Mn}_x\text{MnTaO}_6$ with $x = 0, 0.2, 0.4, 0.6, 0.8$ and

1.0

	$x = 0$	$x = 0.2$	$x = 0.4$	$x = 0.51^a$	$x = 0.8$	$x = 1.0$
(Ca1/Mn2)-O1	2.485 (17)	2.311 (17)	2.073 (10)	2.75 (3)	2.989 (17)	2.894 (17)
(Ca1/Mn2)-O1	2.600 (11)	2.693 (12)	2.631 (16)	2.64 (2)	2.80 (3)	2.73 (3)
(Ca1/Mn2)-O2 ($\times 2$)	2.110 (9)	2.166 (11)	2.473 (7)	2.29 (2)	2.33 (2)	2.372 (17)
(Ca1/Mn2)-O2 ($\times 2$)	2.807 (10)	2.805 (11)	2.617 (7)	2.634 (15)	2.42 (3)	2.450 (15)
(Ca1/Mn2)-O2 ($\times 2$)	2.938 (8)	2.868 (11)	2.859 (7)	2.89 (2)	3.09 (3)	2.961 (18)
<(Ca1/Mn2)-O1>	2.543 (14)	2.502 (15)	2.352 (13)	2.695 (3)	2.895 (10)	2.812 (10)
<(Ca1/Mn2)-O2>	2.618 (9)	2.613 (11)	2.650 (7)	2.605 (6)	2.613 (3)	2.594 (17)
<(Ca1/Mn2)-O>	2.599 (10)	2.585 (12)	2.575 (9)	2.627 (5)	2.684 (5)	2.649 (15)
BVS(Ca1)	2.14	2.09	1.95	1.61	1.60	1.56
BVS(Mn2)	-	1.29	1.21	1.00	0.99	0.96
BVS(Ca1/Mn2)	2.14	2.01	1.80	1.43	1.36	1.26
(Mn1/Ta1)-O1 ($\times 2$)	1.9565 (17)	1.982 (3)	1.999 (2)	1.953 (4)	1.949 (4)	1.940 (3)
(Mn1/Ta1)-O2 ($\times 2$)	1.977 (10)	1.967 (10)	1.950 (7)	1.98 (3)	1.98 (4)	1.944 (18)
(Mn1/Ta1)-O2 ($\times 2$)	2.053 (9)	2.035 (10)	2.029 (7)	2.09 (2)	2.06 (3)	2.06 (2)
<(Mn1/Ta1)-O1>	1.9565 (17)	1.982 (3)	1.999 (2)	1.953 (4)	1.949 (4)	1.940 (3)
<(Mn1/Ta1)-O2>	2.015 (10)	2.001 (10)	1.990 (7)	2.035 (3)	2.020 (4)	2.002 (10)
<(Mn1/Ta1)-O>	1.996 (12)	1.995 (8)	1.993 (5)	2.008 (3)	1.996 (4)	1.981 (8)
BVS(Mn1)	3.19	3.19	3.21	3.11	3.19	3.33

^aThe data for $x = 0.51$ phase is shown only in the $x = 0.6$ case.

Table 3. Magnetic parameters for $\text{Ca}_{2-x}\text{Mn}_x\text{MnTaO}_6$ ($x = 0\text{-}1.0$) measured in 0.1 T magnetic field

Compound	θ_{W} (K)	$T_{\text{C}}/T_{\text{N}}$ (K)	μ_{eff} ($\mu_{\text{B}}/\text{f.u.}$)	μ_{cal} ($\mu_{\text{B}}/\text{f.u.}$)
$x = 0$	39.4	19.6	5.33	4.90
$x = 0.2$	23.4	44.0	5.37	5.57
$x = 0.4$	-64.6	11.6	7.69	6.14
$x = 0.6$	-108	16.6	7.59	6.71
$x = 0.8$	-149	22.5	7.94	7.21
$x = 1.0$	-260	23.3	9.55	7.68

Table of Contents Graphic

